<sup>1</sup>Lian Lu <sup>2</sup>Zhi Zhang

# Interactive Visualization of Hyperspectral Images in Sustainable Environments Using Machine Learning



Abstract: - In the endeavour to achieve sustainable development objectives, the notion of smart cities has gained significant importance in recent times. New ideas for more sustainable cities have generally surfaced as a result of smart-city services addressing prevalent urban issues. One of the most important topics in realm of remote sensing is categorization of hyperspectral images (HSI). For conventional machine learning (ML) models, the classification process is quite difficult since HSI typically needs to cope with complicated features and nonlinearity among the hyperspectral data. Aim of this research is to propose novel technique in urban area green region analysis based on hyperspectral imaging in geographical information system using machine learning and smart grid for sustainable city application. Here the IoT based environmental monitoring sensor integrated with smart grid has been used in urban area green region analysis. Then through IoT module the monitored sensor hyperspectral images has been collected and processed for analysing the green region using graph convolutional U-net adversarial neural network. experimental analysis has been carried out based on various hyperspectral images in terms of training accuracy, precision, sensitivity and Normalized square error. Then the analysis of smart grid module is carried out in terms of throughput, end-end delay, packet delivery ratio, QoS. Proposed technique training accuracy 97%, precision 96%, Normalized square error of 58% and sensitivity of 95% for hyperspectral image analysis. The proposed GCU-netANN obtained accuracy of 97%, packet delivery ratio of 95%, QoS of 91%, end-end delay of 75% for IoT smart grid network analysis.

*Keywords:* Urban Area, Green Region Analysis, Hyperspectral Imaging, Geographical Information System, Machine Learning, Smart Grid

#### 1. Introduction:

Driven by global pursuit of Sustainable Development Goals (SDGs) set forth by United Nations, idea of smart cities has become a central paradigm in urban development in recent years. There is an inevitable rise in demand for smart urban services as a result of the complex issues that cities face as a result of the extraordinary rate of urbanisation [1]. This unfavourable situation gives rise to the idea of "smart cities," which provide a picture of intelligent, environmentally responsible, and socially inclusive urban settings. The smart-city model now includes sustainability as a distinguishing concept. Way cities are planned as well as designed has drastically changed as a result of realisation that resource conservation, environmental stewardship, and the enhancement of quality of life are crucial elements of urban growth. As a result, the pursuit of the SDGs and worldwide worries about climate change and environmental degradation have made it more and more important to turn metropolitan areas into smart cities that put the welfare of their residents and the surrounding ecosystems first [2]. Typical urban problems such as energy inefficiency, inadequate infrastructure to mitigate pollution, and traffic congestion have been evaluated for optimisations supported by smart-city services. Aside from the general notion of "improvement" that has been heavily promoted by huge corporations and governments, smart cities can play a pivotal role in steering the pressing sustainable revolution in our urban areas. To put it briefly, smarter cities may be built around a more harmonic and comprehensive interaction between people and their urban surroundings, even while smart services can maximise resource utilisation and minimise waste and pollution [3]. The goal of hyperspectral imaging as a remote sensing approach is to extract meaningful information from images that are taken by sensors that perform hyperspectral imaging. The HSI sensors gather electromagnetic radiation from the same region of the earth's surface that is reflective and has hundreds of extremely small spectral bands. In a hyperspectral image, each pixel may be thought of as a vector that contains the spectral reflectance of a material at a particular wavelength. Every pixel in the hypercube has a distinct spectral signature due to this spectrum reflectance, and these spectral signatures are utilized to distinguish between different types of materials found on the surface of the planet. As a result, HSI has been applied in many other domains, including medical science, agriculture, land cover, and remote sensing [4]. The spectrum, which is a vector made up of hundreds of elements that measures

<sup>&</sup>lt;sup>11</sup> School of Finance and Business, Zhongshan Torch Polytechnic, ZhongShan,528436, China. <u>lulian198008@163.com</u>

<sup>&</sup>lt;sup>2</sup>School of Photoelectric Information, Zhongshan Torch Polytechnic, ZhongShan,528436, China. <u>zhangzhi198910@163.com</u>

energy emitted or reflected as a function of wavelength, is what makes up each pixel in a hyperspectral image. Therefore, it is possible to think of a hyperspectral image as a three-dimensional data structure that has one spectral axis that contains information about the chemical composition of the objects and two spatial axes that carry information about the location of the objects. Since the atomic or molecular structure of a material determines how light at different wavelengths interacts with it, the spectrum records the chemical information [5]. Hyperspectral sensors installed on satellites and aircraft can identify and locate things, map the land use and cover, and comprehend the physical characteristics of materials over a wide geographic area. The primary goal of early HSI classification research has been to investigate spectral fingerprints of HSIs using pixel-wise classification techniques such as logistic regression (LR), support vector machines (SVM), neural networks (NN). In addition, other classification approaches have focused on extracting high-level features and reducing dimensions using methods like principal component analysis (PCA), independent component analysis (ICA), linear component analysis (LDA). However, because these approaches do not take geographical information into account, the classification accuracies have not proven adequate. In several approaches, the incorporation of spatial information alongside spectral information has been observed to be beneficial in enhancing classification accuracies. However, in the aforementioned approaches, extracting discriminative features from HSIs has proven to be an extremely important task [6].

## 2. Background and related works:

Recent years have seen the successful application of several ML as well as DL, including convolutional neural networks (CNN), support vector machine regression (SVR), partial least squares regression (PLSR), NN, random forests (RF), to a variety of agricultural condition monitoring, plant disease and insect monitoring, wheat ear identification, other areas. For instance, work [7] employed CNN to identify and track pest insects and plant illnesses. In order to obtain precise segmentation as well as recognition of quantity of wheat ears, author [8] employed CNN. In [9], spectral characteristics were collected from UAV hyperspectral data, and PLSR was used to build the winter wheat LAI estimation model. Work [10] used VIs, RF, and PLSR to build an estimating model for wheat LAI. The derived spectrum parameters and machine learning methods are integrated in the previously stated studies to create inversion models of physiological parameters. Recently, investigations on ground monitoring or satellite remote sensing have made extensive use of spectral feature extraction methods such principal component analysis (PCA), variable projection importance (VIP), genetic algorithm (GA), continuous projection algorithm (SPA). By effectively eliminating redundancy in hyperspectral data, these algorithms can lower the likelihood of overfitting and ultimately produce a model with a strong and high prediction accuracy [11]. The spectrum data acquired are inconsistent as a result of sensor performance variance. Author [12] showed that spectral reflectance properties alone might be used to quickly distinguish between healthy leaves and commercial maize kernels infected with toxigenic fungus. Three sugar beet diseases—cercospora leaf spot, powdery mildew, leaf rust—were distinguished by work [13] using spectral angle mapper and hyperspectral imaging techniques. Author [14] looked at the potential use of hyperspectral imaging to identify two distinct tomato leaf diseases: early and late blight. An extreme learning machine method was created to classify healthy plants, early blight, late blight of detached leaves. Based on spectral information, the model was able to detect diseased plants with an accuracy of 97.1-100%. The accuracy of the texture analysis was roughly 70%. However, aforementioned studies consistently ignored significance of data fusion in favour of a standard ML method based on spectral signature. There aren't many extensive studies on the use of HSI with spectral analysis, texture analysis, data fusion to distinguish between early-stage infected and non-infected leaves and classify various disease severity levels. ELM as well as ideally pruned ELM (OP-ELM) were used in [15] to classify soybean varieties using hyperspectral photos. Using two datasets, ELM produced classification accuracies for land cover that were comparable to those of a back-propagation neural network [16]. In [17], KELM was applied to the categorization of multi- and hyperspectral remote sensing pictures. According to results, KELM offers noticeably low computational cost and classification accuracy comparable to or higher than SVMs. But in these publications, ELM was used as a pixel-wise classifier, meaning that spatial information at nearby sites has been ignored and just spectral signature has been used. However, for HSI, likelihood of two neighbouring pixels being in the same class is very high. It has been demonstrated that taking into account both spectral as well as spatial data greatly increases HSI classification accuracy. Spatial features can be used in two main ways: either to extract specific types of spatial features or to use nearby pixels directly for joint classification, presuming that these pixels

typically belong to same class. Because Gabor features can convey meaningful spatial information, they are successfully used for hyperspectral image classification in the first category. Three-dimensional (3-D) Gabor filters were utilized in [18] to extract 3-D Gabor features from hyperspectral pictures; two-dimensional (2-D) Gabor features were extracted in a subspace projected by PCA. Both supervised and unsupervised learning were used in a hybrid strategy that was suggested [19]. When it came to unsupervised learning, the information gathered from this approach outperformed deep learning-based HIS categorization based on spectral-spatial features. The suggested unsupervised method for Deep Feature Extraction [20] yielded superior results compared to the current cutting-edge algorithms, principal component analysis (PCA), kernel counterpart (kPCA), and certain aerial classification techniques. The suggested method is more effective at teaching data representations. The technique used a single-layer convolution network to achieve high resolution and detailed neighbour pixel results. Furthermore, it performs better when it comes to features with complexity and abstraction levels as well as singlelayer variations. The suggested method extracted features in the style of unsupervised learning using the 3-D Convolutional Autoencoder (3D-CAE) [21] without training labelling the data. In order to learn the sensorspecific characteristics, the models extended the unsupervised spatial-spectral feature extraction onto multiple images captured by the same sensor. The model therefore learns the spatial-spectral properties of HSI under the unsupervised measurement. SVM as well as partial least squares discriminant analysis are regarded as most dependable methods among them. This is especially true when there aren't many training data available. Image classification has made extensive use of machine learning. One of the benefits of using Multilayer Perceptrons (MLP) techniques is their ability to handle enormous amounts of training data [22]. While producing results on the HSI classification procedure that were equivalent to those of other methods, these techniques could automatically learn features. The target, or weeds, as well as the background and other elements that can have an impact on the target species' labelling accuracy, are typically present in the original HSI image.

# 3. IoT based sensor integrated with smart grid in urban area green region analysis:

The detailed description of the suggested IoT sensor-based smart monitoring as well as controlling paradigm for smart grid systems is given in this section. This work's primary contribution is the use of an Internet of Things-based wireless communication network for smart grid system monitoring and control. It also encourages the enhancement of high-reliability and voltage-profile smart grid systems' power quality. Smart sensors are often regarded as most crucial Internet of Things (IoT) devices for enhancing dependability of smart grid systems. A smart sensor is a type of device that gathers environmental data and relays it to controlling systems. Here, the main goals of employing smart sensors are to improve system quality and dependability while effectively managing anomalous circumstances in smart grid systems. Figure 1 displays architecture representation of smart grid methods.

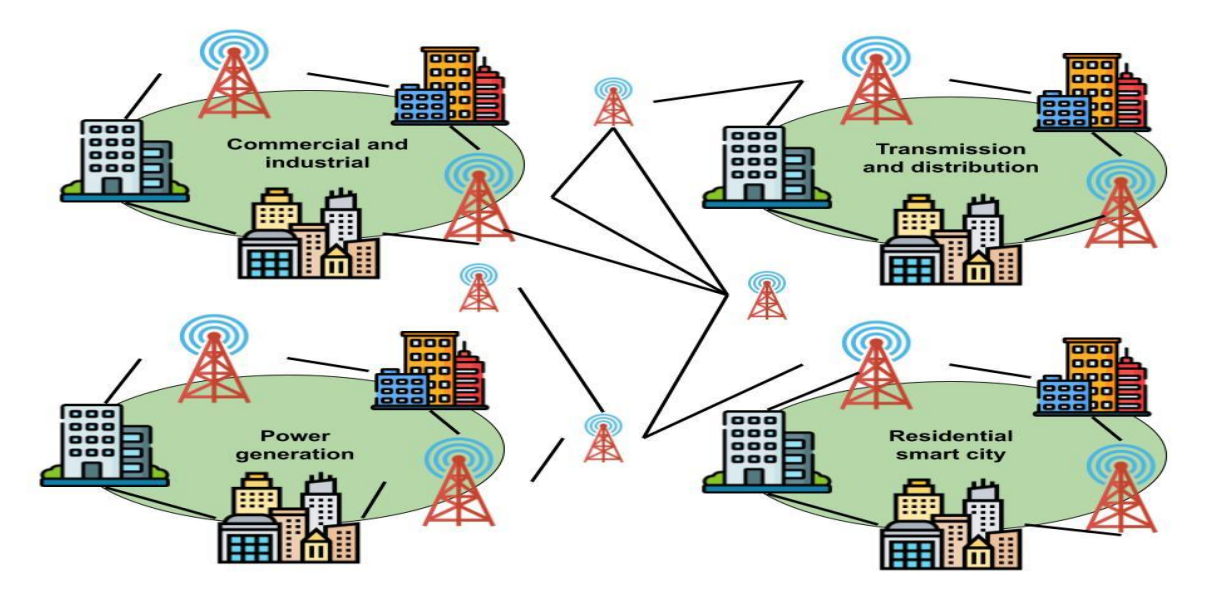


Figure 1 Smart grid IoT architecture

The three main components of the suggested framework are the components for analysis, communication, and monitoring. The suggested framework's monitoring element is made up of voltage and current sensors that are fastened to consumer loads. Other two main components are the analytical and communication components. Subsequently, the communication component consists of the WiFi module and Arduino sensor, which provide wireless connection. Here, voltage profiles, energy reports, voltage, current are obtained via analysis component, which is utilised as a remote application. The cloud-based application system at the power grid's substation assesses the real-time target demand against the actual target and adjusts to deliver services like remote power supply and security management. The substation-connected assets were monitored, analysed, and shared with information via the Internet of Everything (IoE). Following the completion of the data analysis process, the appropriate party will grant permission to carry out the necessary steps, transforming power plant as well as SG from a traditional into a virtual method. The sophisticated distributed energy management system's power consumption efficiency is increased through the use of technology. Utilising pertinent optimisation techniques at various stages maximises output while lowering costs, boosting profitability, enhancing dependability, and integrating more renewable resources into SG network [16]. A select group of sophisticated applications, such as distributed energy resource management methods, low voltage outage management systems, sub-station device management, grid analytics, and smart metre data management, are integrated with Internet of Everything. Through integration of devices and real-time data, SG enables the secure and quick delivery of power and information to the digital world. The smart energy infrastructure, which includes automated and centralised distribution systems, energy metering units, energy storage devices, loads, is depicted in Figure 2 as an interconnected network.

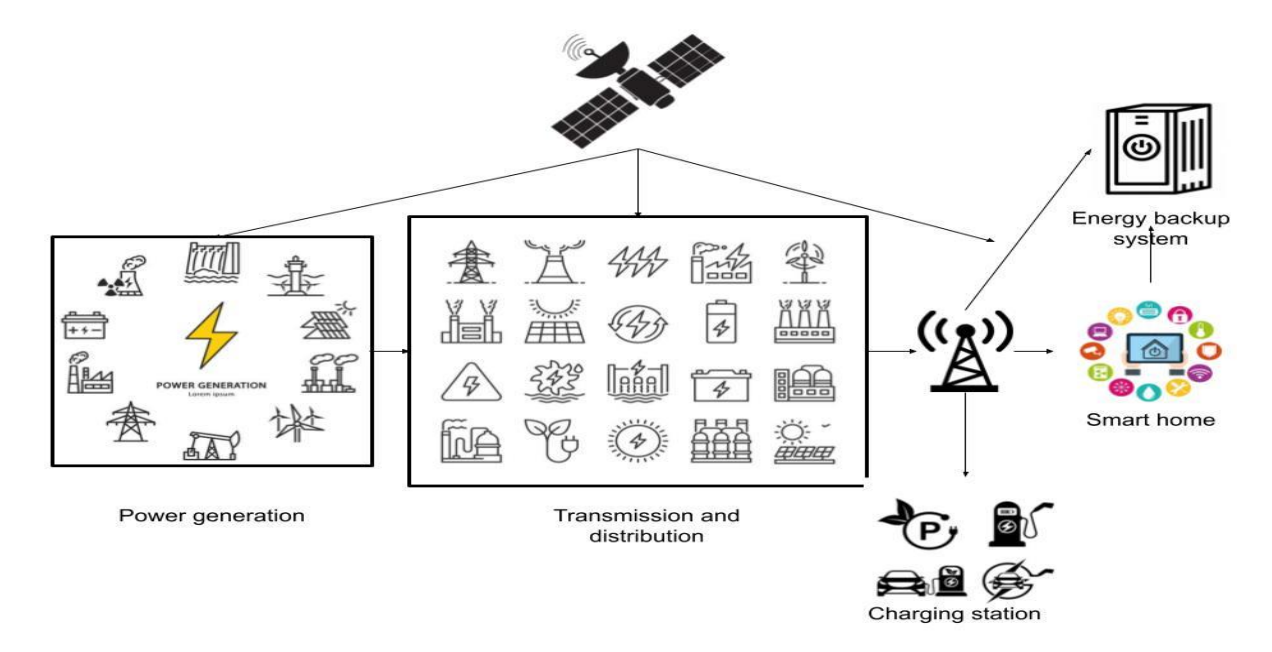


Figure 2 IoT-based efficient energy transaction at grid and charging stations

# 4. Hyperspectral images based green region analysis using graph convolutional U-net adversarial neural network (GCU-netANN):

We take advantage of the fact that graph convolutions are permutation equivariant and stable to graph perturbations to arrive at a stability conclusion for GRNN. We can assess target representation Y by using the fact that concealed state zt is a graph signal. In order to do this, we use a GNN ( $\Phi(z_t;S)$ ) to produce the estimate Y^.When yt is a graph signal by itself,  $\rho$  can be the activation function by using equation (1), and  $\Pi$  is a simple one-layer graph filter.

$$\hat{\mathbf{y}}_t = \rho(\mathbf{C}(\mathbf{S})\mathbf{z}_t) \tag{1}$$

Graph signaling concealed state zt has several advantages. First of all, it improves the interpretability of the signal's value with respect to the underlying graph support. For instance, we may look at the frequency content of

the hidden state and compare it to the frequency content of the graph process xt. Second, it allows zt to be computed entirely locally, requiring just recurrent exchanges with the one-hop neighbors of each node. But converting zt to a graph signal also means that the size of the concealed state, now set at N, cannot be changed. One important hyperparameter in the creation of RNNs is the size of hidden state, as it controls the HMM's description capabilities. Graph signal tensors, which assign a vector of features to each node instead of a single scalar, are introduced to address this. An operation. A graph signal tensor is X:V $\rightarrow$ R $^$ F that assigns a vector of dimension F to each node. This map is implemented by a bank of F G graph filters of rank K; filter taps are provided by  $\mathbf{a}\mathbf{a}_n^{fg} = [a_0^{fg}, \dots, a_{K-1}^{fg}]$ . Equation (2) describes the convolution of graph  $\mathcal{A}_S$ :  $\mathbb{R}^{N\times F} \rightarrow \mathbb{R}^{N\times G}$ .

$$\mathbf{Y} = \mathcal{A}_{\mathbf{S}}(\mathbf{X}) = \sum_{k=0}^{K-1} \mathbf{S}^k \mathbf{X} \mathbf{A}_k \tag{2}$$

where  $A_k$  is a matrix that satisfies  $A_k \in \mathbb{R}^{F \times H}$  in this case. It is evident that left-hand operations that modify X must respect the graph's sparsity for convolution to stay local on the graph, whereas right-hand operations can modify it in any linear way. The purpose of the relevant procedures is to apply the same linear combination—parameter sharing—to each node by eqn (3) in order to integrate characteristics inside a single node.

$$\mathbf{Z}_{t} = \sigma \left( \mathcal{A}_{\mathbf{S}}(\mathbf{X}_{t}) + \mathcal{B}_{\mathbf{S}}(\mathbf{Z}_{t-1}) \right) \tag{3}$$

$$\mathbf{Y}_t = \rho \big( \mathcal{C}_{\mathbf{S}}(\mathbf{Z}_t) \big) \tag{4}$$

with filter taps  $\mathbf{C}_k \in \mathbb{R}^{G \times H}$  ,  $k = 0, \dots, K-1$ 

By describing the hidden state with graph signal tensors, we regain the ability to alter its descriptive strength through the value of H. Remember that each node's distinct hidden state feature values can be used directly to produce the output Yt, which lowers communication costs. In this architecture, node contacts are only required for updates of the concealed state Zt.

A 2D-CNN typically uses two activation functions: softmax for the output layer and rectified linear unit (ReLu) for the other layers. Softmax uses output scaling between zero and one to provide a likelihood of coverage falling into a given class. ReLu is a linear function that will output the value immediately if the input is positive. Anything else will result in zero. Additionally, CNN 1 consists of a max-pooling layer that follows three convolutional layers in order. Figure 3 displays a graphical depiction of the CNN architecture.

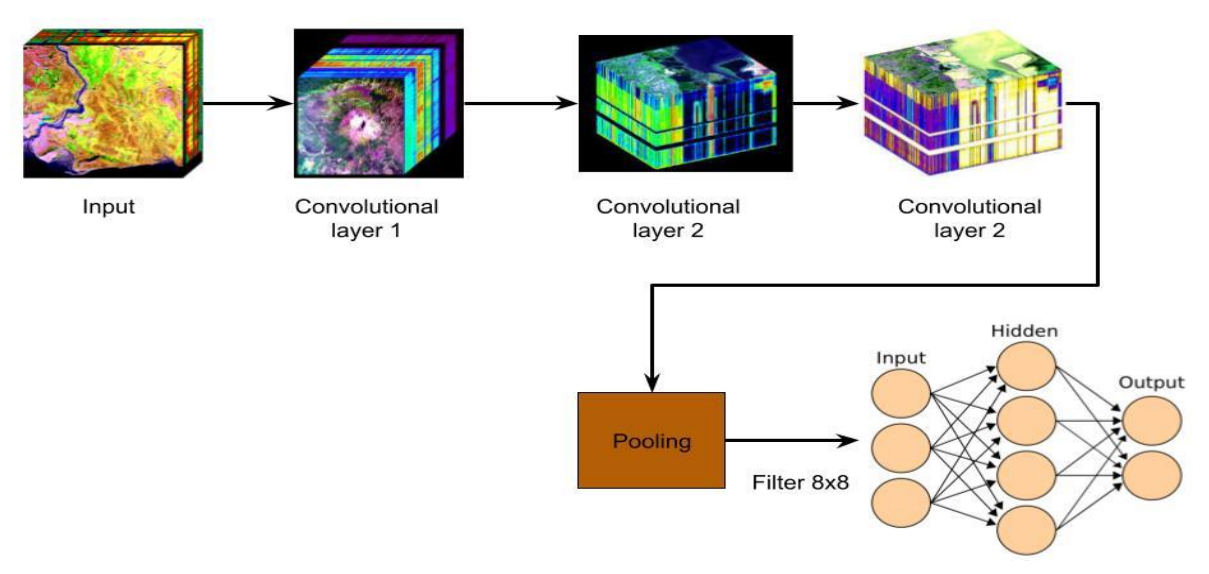


Figure 3. A schematic view of the proposed CNN.

By performing the convolution process over the whole input matrix, emotion features are extracted from the N-grams that the filters convolved themselves with. The learning of weights F and biases b is first phase in the

convolutional layer training process. This is a non-linear function, g, which is the hyperbolic tangent in our experiment. This is how a feature ci is created by eqn (5)

$$Ci = g(F * wi + h - 1 + b) \tag{5}$$

All of the N-grams of size h in the sentence are located by filtering the segmented sequence of length n, {w1:h,w2:h+1, ..., wn-h+1:n}. For every input sentence, the filtering procedure thus produces a feature of size n-h+1. A series of filters creates feature maps; a pooling process is needed to extract the most sensitive responses across features. In this work, we apply different sized filters to extract features from different sentence viewpoints.

Pooling: Subsequently, feature maps are sent to the layer in charge of pooling operations, allowing the best solutions to be combined while maintaining the sequential information within the feature. Equation (6) is used to determine the highest feature value (cmax) on map C using the max-overtime pooling strategy.

$$c_{\max} = \max\{C\} = \max\{c_1, \cdots, c_{n-h+1}\}$$

$$\frac{\partial}{\partial w_{ij}^{(0)}} J_{NSCDNN}(\boldsymbol{W}, \boldsymbol{b}) = \frac{\partial}{\partial w_{ij}^{(0)}} J_{E}(\boldsymbol{W}, \boldsymbol{b}) + \beta \frac{\partial}{\partial w_{ij}^{(h)}} J_{KL}(p \parallel \hat{\boldsymbol{p}}) + \alpha g(w_{ij}^{(i)})$$

Where

$$g(x) = \begin{cases} w_{ij} & w_{ij} < 0\\ 0 & w_{ij} \ge 0 \end{cases}$$
 (6)

The non-negative constrained softmax classifier's cost function is defined as eqn (7) as, in accordance with our methodology, non-negative constraints are also imposed to the classifier's weights during training.

$$J_{NC-S_{eft}\max}(\mathbf{W}) = J_{CL}(\mathbf{W}) + \frac{\alpha}{2} \sum_{i=1}^{x_L} \sum_{j=1}^{k} f(w_{ij}^{(L)})$$
 (7)

The final step in deep network training is fine-tuning the network for optimal classification in a supervised mode. Equation (8) represents the deep network's fine-tuning cost function.

$$J_{DN}(\boldsymbol{W}, \boldsymbol{b}) = J_{CL-DN}(\boldsymbol{W}_{DN}, \boldsymbol{b}_{DN}) + \frac{\alpha}{2} \sum_{i=1}^{s_L} \sum_{j=1}^{k} f(w_{ij}^{(L)})$$
(8)

In this case,  $L(\theta, \varphi; xi)$  can be the form formulated by Eqn. (9).

$$\mathcal{L}(\boldsymbol{\theta}, \boldsymbol{\phi}; \boldsymbol{x}_i) \simeq \frac{1}{2} \sum_{j=1}^{J} \left( 1 + \log \sigma_{i,j}^2 - \mu_{i,j}^2 - \sigma_{i,j}^2 \right) + \frac{1}{I} \sum_{l=1}^{L} \log p(\boldsymbol{x}_i \mid \boldsymbol{z}_l; \boldsymbol{\theta})$$
(9)

where the outputs of the VAEs' encoder are distribution parameters mean  $\mu i$  and variance  $\sigma$  2 i. Moreover, J stands for underlying manifold's dimensionality, L represents sample size utilized in Monte Carlo approach for sampling from estimated posterior distributions.

The total number of training movies that include both the motion and spatial representations is denoted by N. n-th sample is expressed as a 3-tuple as (xs n, xm n, yn), where averaged spatial and motion features are given by  $\mathbf{x}_n^s = \sum_{t=1}^T \mathbf{x}_{n,t}^s \in \mathbb{R}^{d_s}$  and  $\mathbf{x}_n^m = \sum_{t=1}^T \mathbf{x}_{n,t}^m \in \mathbb{R}^{d_m}$  and corresponding label of n-th sample. Let's start by discussing a degraded scenario, in which there is only one feature available, for the sake of clarity by eqn (10)

$$\min_{\mathbf{W}} \sum_{i=1}^{N} \| g(\mathbf{x}_i) - \mathbf{v}_i \|^2 + \lambda_1 \Phi(\mathbf{W})$$
 (10)

where the second component is often a regularizer based on the Frobenius norm to prevent over-fitting, first term quantifies difference between output g(xi) and ground-truth label yi. Situation of fusion as well as prediction with two features is what we will talk about next. It should be noted that the method is easily expandable to accommodate more than two input features.

The discriminator network and generator network are the two subnetworks that make up a GAN's architecture. The generator network creates artificial images by obtaining visual features. As opposed to this, the discriminator

network gathers artificial images, separates them from real photos, then adjusts loss function until created and real images are identical. To simplify the model architecture and lower the time complexity of implementing our model without compromising model features, we treat the autoencoder module's decoder network as the GAN module's generator network. Furthermore, decoder network produces image samples for minority classes, just as GAN module's generating network ought to. So, the discriminator network is our main concern. The design of discriminator network is shown in Figure 6.

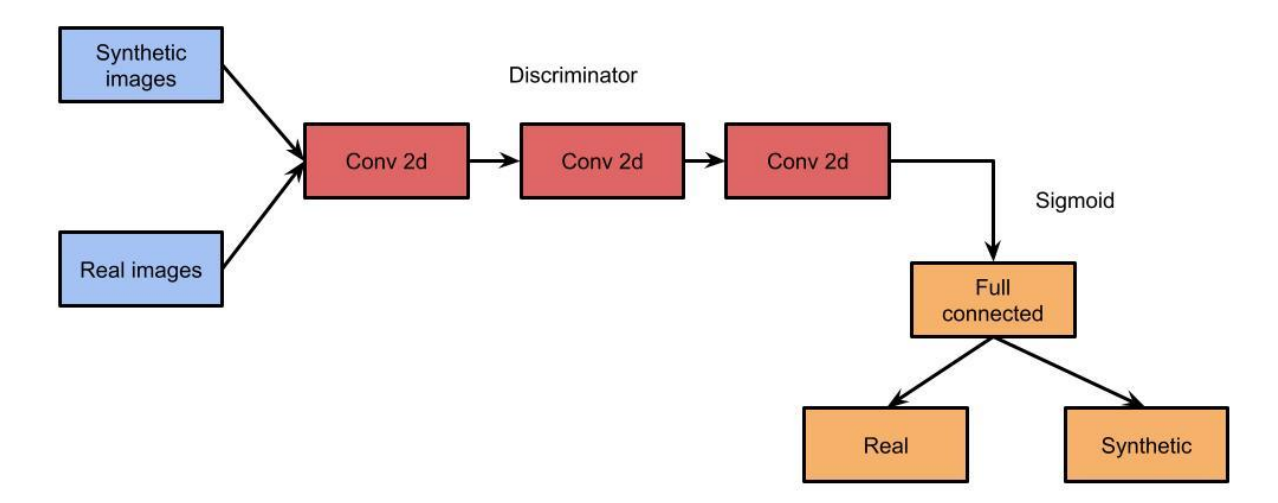


Figure 4. The illustration of the discriminator network.

According to Figure 4, There are three convolution layers in the discriminator network, and they are all two-dimensional layers. ReLU activation is applied in first and second layers, while sigmoid activation is used in final layer to differentiate between genuine and synthetic image types. The only distinction between the classifier and discriminator networks' designs is the usage of the SoftMax function in the final convolution layer. The SoftMax loss value is derived from the classifier network's computation of each image class's scores. The following is how the categorization network's training and testing procedures are put into practice. Testing data is used to verify classification accuracy for every classification method, and training samples of every balanced image class were used to carry out the classification procedure.

# 5. Experimental analysis:

In this study, hyperspectral image classification method is proposed and the proposed method is tested. We have done all our experiments by utilizing Python 2.7with Spyder Integrated Development Environment(IDE) and Keras and TensorFlow frameworks utilizing deviceGforceGTX 770, CUDNN 5110. We assess performance of our watermarking framework with standard datasetwith learning ratee of 0.5. We trained our method on multipleepochs. Every time it gives almost same error rate as well as same accuracy.

Datasets: To evaluate the efficacy of our model, we employed four hyperspectral unbalanced datasets from different environments: Salinas, Botswana, Kennedy Space Centre, Indian Pines, and Salinas. The datasets are described briefly here.

1. In the Indian Pines region of Indiana, the AVIRIS sensor is used to gather the Indian Pines dataset. There are 224 bands in collection, their wavelength range is  $0.4-2.5 \times 10-6$  m. The image measures 145 by 145 pixels. Table 1 provides further information about the classes and samples of Indian Pines.

Table 1. Classes information of Indian Pines dataset.

Number	Land Cover Class	Samples	
1	Alfalfa	46	

2	Corn	237
3	Corn-mintill	830
4	Corn notill	1428
5	Grass-pasture	483
6	Hay-windrowed	478
7	Grass-pasture-mowed	28
8	Grass-trees	730
9	Oats	20
10	Soybean-notill	972

2. In the Californian Salinas region, the AVIRIS sensor is used to gather the Salinas dataset. The picture size of the Salinas dataset is  $512 \times 217$  pixels, with 204 bands. Table 2 provides more information regarding land cover classes in Salinas dataset, including samples.

Table 2. Classes information of Salinas dataset.

Number	Land Cover Class	Samples
1	Fallow	1976
2	Brocoli_green_weeds_2	3726
3	Brocoli_green_weeds_1	2009
4	Fallow_rough_plow	1394
5	Celery	3579
6	Stubble	3959
7	Fallow_smooth	2678
8	Grapes_untrained	11,271
9	Corn_senesced_green_weeds	3278
10	Soil_vinyard_develop	6203

3. NASA AVIRIS is used at Kennedy Space Centre location in Florida to collect Kennedy Space Centre dataset. KSC dataset has  $512 \times 614$  pixel images with 224 spectral reflectance bands. The KSC dataset's classes and sample details were reported in Table 3.

Table 3. Classes information of KSC dataset.

Number	Land Cover Class	Samples
1	CP hammock	256
2	Willow swamp	243
3	Scrub	761

4	Slash Pine	252
5	Swap	105
6	Hardwood	229
7	Oak/Broadleaf	161
8	Graminoid marsh	431
9	Cattail marsh	404
10	Spartina marsh	520

Training Settings: Our suggested model's layer weights were initialised at random, and the Adam optimizer was used to update the model's parameters together with a 0.0002 learning rate. For every dataset, 400 epochs was the maximum number that could be used. Every trial in our method training phase was ran through 4000 iterations, and the procedure came to an end when the artificial images of the minority classes' generalisation stabilised. For each of the four datasets, a  $25 \times 25 \times D$  spatial window was chosen, with D standing for the number of bands. For every dataset, there were varying numbers of samples used in the training and testing phases. For instance, Soybean-mintill was deemed the majority class since Indian Pines had greatest number of samples. 1500 samples were used in experiment as sample size for actual training dataset. Some classes were deemed minority classes, meaning they had to provide artificial samples as well as adjust each minority class's sample size. For every dataset, the number of testing samples is equal to one-fourth of the training samples. Due to their high degree of inter-band correlation, hyperspectral images are considered high-dimensional data. This might lead to information redundancy as wekk as instability in multivariate prediction methods convergence. Using fewer wavebands will result in more stable models as well as make multispectral imaging method that follows easier to build.

Table-4 Comparative analysis in Hyperspectral image classification for various datasets

Dataset	Hyperspectral Input Image	Processed image	urban area based green region analysis
Indian Pines dataset			
Salinas dataset			
KSC dataset			

A comparative comparison of hyperspectral image categorization for different input datasets is presented in Table 4 above. Based on the image classification used to distinguish the land surfaces from the gathered hyperspectral image, a comparison has been made. The suggested model-based categorization, out of all the methods previously compared, produced an improved and precise output when assessing the input hyperspectral image.

Table-5 Comparative	based on	various	hyperspectral	image dataset
			~ I I	_

Dataset	Techniques	Training accuracy	precision	Normalized square error	Sensitivity
Indian	RFNN	79	78	63	69
Pines	GAN	81	80	57	73
dataset	GCU-netANN	85	85	53	80
SALINAS - dataset	RFNN	84	83	63	83
	GAN	87	88	65	85
uataset	GCU-netANN	90	92	60	90
KSC -dataset -	RFNN	87	87	66	89
	GAN	90	92	63	93
	GCU-netANN	97	96	58	95

Table-5 shows comparative for hyperspectral image dataset, here the dataset compared are Indian Pines dataset, SALINAS dataset, KSC dataset in terms of training accuracy, precision, specificity, Normalized square error and sensitivity.

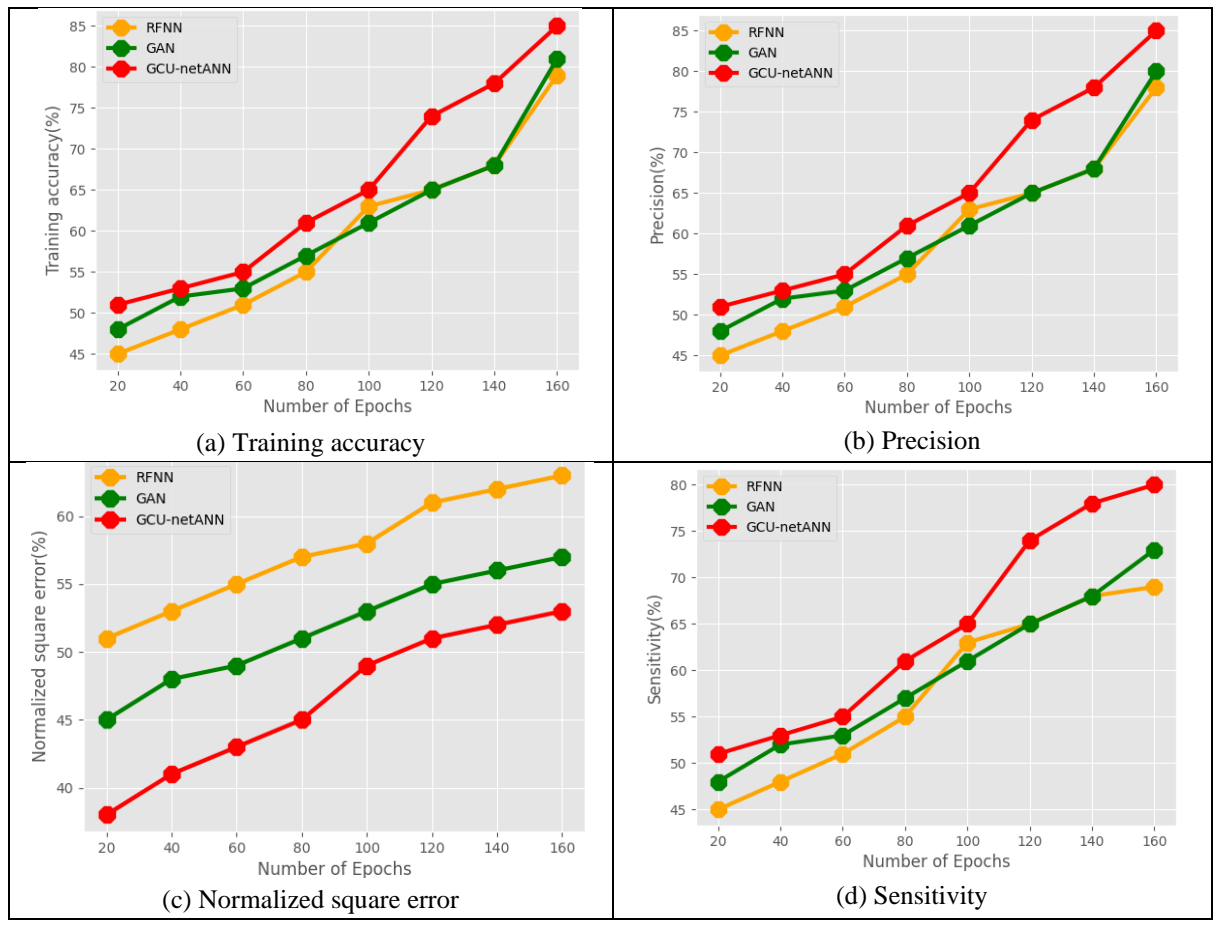


Figure-5 Parametric analysis for Indian Pines dataset, SALINAS dataset, KSC dataset in terms of (a) Training accuracy, (b) Precision, (c) Specificity, (d) Normalized square error, (e) Sensitivity

the above figure 5 shows comparative for Indian Pines dataset. proposed technique attained training accuracy 82%, F\_1 score of 68%, Normalized square error of 73% and sensitivity of 65%, existing RFNN attained training accuracy 77%, precision of 62%, Normalized square error of 68% and sensitivity of 59%, GAN attained training accuracy 79%, precision of 63%, Normalized square error of 72% and sensitivity of 63%. comparative analysis between proposed and existing technique for SALINAS dataset is shown. here the training accuracy attained is 88%, Precision of 71%, Normalized square error of 77% and sensitivity of 73% by proposed technique; while existing RFNN training accuracy 82%, precision 65%, Normalized square error of 73% and sensitivity of 66%, GAN attained training accuracy of 85%, precision of 69%, Normalized square error of 75% and sensitivity of 69%. comparative for KSC dataset. proposed technique attained training accuracy 97%, precision 96%, Normalized square error of 58% and sensitivity 95%, existing RFNN attained training accuracy 85%, precision of 67%, Normalized square error of 76%, sensitivity 69%, GAN attained training accuracy 88%, precision 72%, Normalized square error of 77% and sensitivity of 73%.

TD 11 /	<i>~</i> ·	1 1		
Table 6	Comparisor	hacad or	i emart aric	analyete
1 autc-0	Comparison	i bascu bi	i siliait giit	i amary sis

Techniques	Throughput	Packet Delivery Ratio	QoS	End-End Delay
GAN	91	85	85	83
RFNN	93	89	89	87
GCU-netANN	97	95	91	75

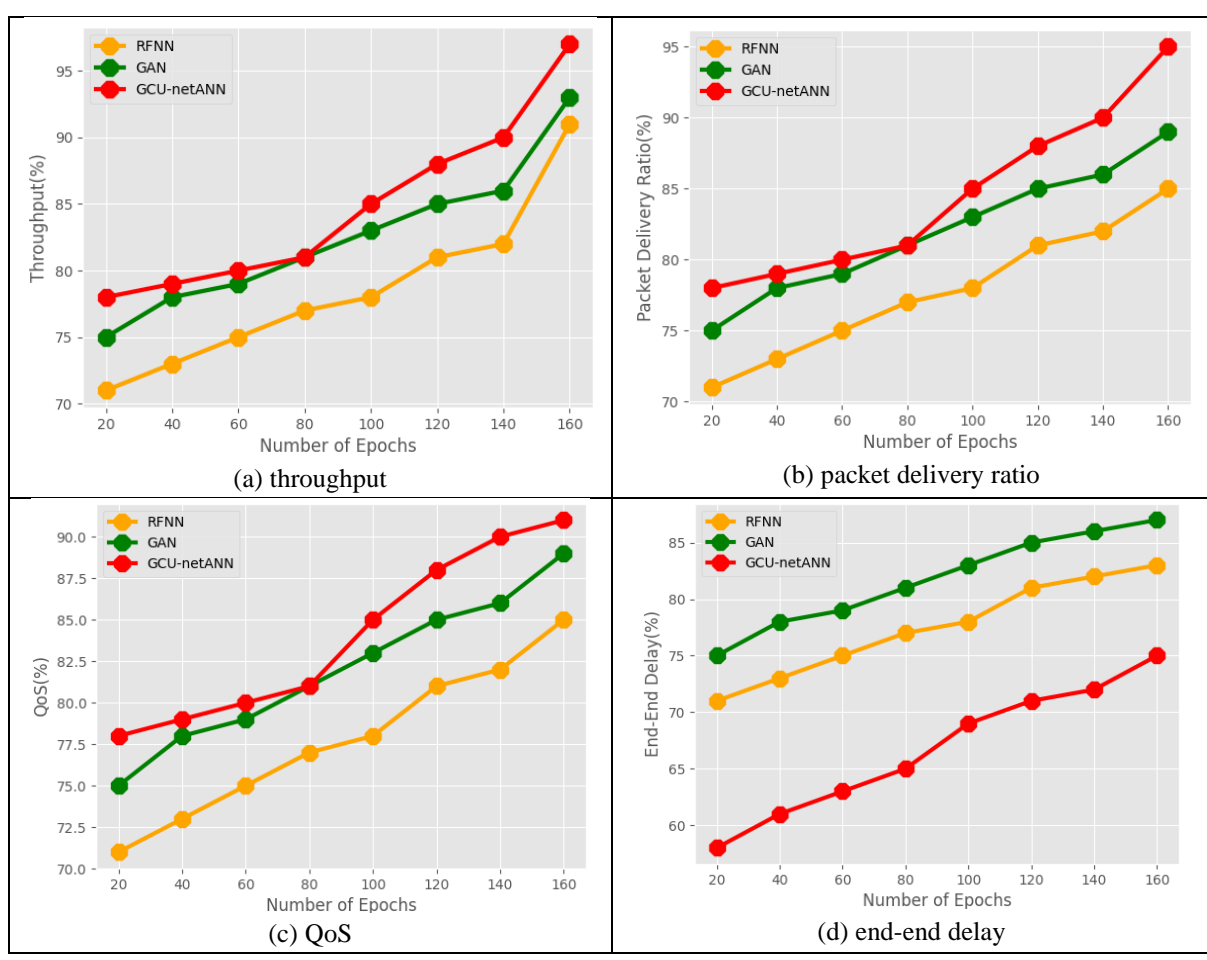


Figure-6 Comparative analysis of Classification in terms of (a) throughput, (b) packet delivery ratio, (c) QoS, (d) end-end delay

Above table-6 shows comparison based on smart grid analysis using machine learning model, here the parametric analysis has been carried out in terms of throughput, packet delivery ratio, QoS, end-end delay. The proposed GCU-netANN obtained accuracy of 97%, packet delivery ratio of 95%, QoS of 91%, end-end delay of 75% as

shown in figure 6 (a)- (e). while existing GAN obtained accuracy of 91%, packet delivery ratio of 85%, QoS of 85%, end-end delay of 87%, RFNN obtained accuracy of 93%, packet delivery ratio of 89%, QoS of 89%, end-end delay of 83%. There are several grayscale images at continuous wavelengths in the hyperspectral cube, also known as the hyperspectral image. Each grayscale image's extracted texture features produce redundant information that is difficult to interpret and unhelpful for early tobacco illness detection. Following that, we used the suggested method to extract four different types of textural features from hyperspectral pictures solely at chosen EWs. To investigate the association between texture variables as well as stage reference values, Pearson correlation (r) was employed.

## 6. Conclusion:

In order to support sustainable city applications, this project aims to present a unique technique for urban area green zone analysis based on hyperspectral imaging in geographic information systems utilising machine learning and smart grid. This urban area green region study makes use of an Internet of Things (IoT)-based environmental monitoring sensor that is integrated with a smart grid. Next, using an adversarial neural network with graph convolution, the monitored sensor hyperspectral pictures were gathered and processed via an IoT module in order to analyse the green zone. Utilising two significant open-source software tools, our work illustrates the potential of hyperspectral analysis for yield and biomass prediction in complex design fields: R language hyperspectral processing package as well as Python's Auto-Sklearn ML technology. We used a variety of hyperspectral vegetation indicators to characterise crop productivity as well as straw bulk, performance evaluation we conducted was satisfactory. We propose that they can be extended to further crop biophysical properties. The application of HSI in plant identification will be greatly advanced by this innovative Sp-based method. When used in grazing fields, especially in mixed swards of a few plant species, this is quite helpful. In order to cope with complicated systems like mixed swards, future study should concentrate on developing a system that enables categorization utilising spectral signature and/or morphological traits linked with decision tree methodologies. More samples with specific spatial metadata can be added to the current database in future studies, enabling more accurate verification using geographic indicators. Samples from various batches, types, seasons, and years, as well as samples from different continents, can all be used for model validation. To validate the concept and identify the selective wavelength zones, more focused analysis are required. In the future, it might be possible to construct an automated system using hyperspectral photography in the field to verify the origin of coffee automatically without handling or destroying samples.

### Reference:

- [1] Ren, H., Xu, C., Ma, Z., & Sun, Y. (2022). A novel 3D-geographic information system and deep learning integrated approach for high-accuracy building rooftop solar energy potential characterization of high-density cities. *Applied Energy*, 306, 117985.
- [2] Ahmad, T., Madonski, R., Zhang, D., Huang, C., & Mujeeb, A. (2022). Data-driven probabilistic machine learning in sustainable smart energy/smart energy systems: Key developments, challenges, and future research opportunities in the context of smart grid paradigm. *Renewable and Sustainable Energy Reviews*, 160, 112128.
- [3] Heidari, A., Navimipour, N. J., & Unal, M. (2022). Applications of ML/DL in the management of smart cities and societies based on new trends in information technologies: A systematic literature review. *Sustainable Cities and Society*, 85, 104089.
- [4] Naqvi, S. A. A., & Naqvi, R. Z. (2021). Geographical Information Systems (GIS) in Industry 4.0: Revolution for Sustainable Development. In *Handbook of Smart Materials, Technologies, and Devices: Applications of Industry* 4.0 (pp. 1-27). Cham: Springer International Publishing.
- [5] Du, B., Mao, D., Wang, Z., Qiu, Z., Yan, H., Feng, K., & Zhang, Z. (2021). Mapping wetland plant communities using unmanned aerial vehicle hyperspectral imagery by comparing object/pixel-based classifications combining multiple machine-learning algorithms. *IEEE Journal of Selected Topics in Applied Earth Observations and Remote Sensing*, 14, 8249-8258.
- [6] Wang, C., Liu, B., Liu, L., Zhu, Y., Hou, J., Liu, P., & Li, X. (2021). A review of deep learning used in the hyperspectral image analysis for agriculture. *Artificial Intelligence Review*, 54(7), 5205-5253.
- [7] Dao, P. D., He, Y., & Proctor, C. (2021). Plant drought impact detection using ultra-high spatial resolution hyperspectral images and machine learning. *International Journal of Applied Earth Observation and Geoinformation*, 102, 102364.

- [8] Yu, R., Luo, Y., Zhou, Q., Zhang, X., Wu, D., & Ren, L. (2021). A machine learning algorithm to detect pine wilt disease using UAV-based hyperspectral imagery and LiDAR data at the tree level. *International Journal of Applied Earth Observation and Geoinformation*, 101, 102363.
- [9] Jaiswal, G., Sharma, A., & Yadav, S. K. (2021). Critical insights into modern hyperspectral image applications through deep learning. *Wiley Interdisciplinary Reviews: Data Mining and Knowledge Discovery*, 11(6), e1426.
- [10] Sim, J., Dixit, Y., Mcgoverin, C., Oey, I., Frew, R., Reis, M. M., & Kebede, B. (2024). Machine learning-driven hyperspectral imaging for non-destructive origin verification of green coffee beans across continents, countries, and regions. *Food Control*, 156, 110159.
- [11] Feng, X., Zhan, Y., Wang, Q., Yang, X., Yu, C., Wang, H., ... & He, Y. (2020). Hyperspectral imaging combined with machine learning as a tool to obtain high-throughput plant salt-stress phenotyping. *The Plant Journal*, 101(6), 1448-1461.
- [12] Farmonov, N., Amankulova, K., Szatmári, J., Sharifi, A., Abbasi-Moghadam, D., Nejad, S. M. M., & Mucsi, L. (2023). Crop type classification by DESIS hyperspectral imagery and machine learning algorithms. *IEEE Journal of selected topics in applied earth observations and remote sensing*, 16, 1576-1588.
- [13] Akar, O., & Tunc Gormus, E. (2022). Land use/land cover mapping from airborne hyperspectral images with machine learning algorithms and contextual information. *Geocarto International*, *37*(14), 3963-3990.
- [14] Pereira, J. F. Q., Pimentel, M. F., Amigo, J. M., & Honorato, R. S. (2020). Detection and identification of Cannabis sativa L. using near infrared hyperspectral imaging and machine learning methods. A feasibility study. *Spectrochimica Acta Part A: Molecular and Biomolecular Spectroscopy*, 237, 118385.
- [15] Liu, Y., Feng, H., Yue, J., Fan, Y., Jin, X., Zhao, Y., ... & Yang, G. (2022). Estimation of potato above-ground biomass using UAV-based hyperspectral images and machine-learning regression. *Remote Sensing*, 14(21), 5449.
- [16] Appeltans, S., Pieters, J. G., & Mouazen, A. M. (2021). Detection of leek white tip disease under field conditions using hyperspectral proximal sensing and supervised machine learning. *Computers and Electronics in Agriculture*, 190, 106453.
- [17] Yang, D., Jiang, J., Jie, Y., Li, Q., & Shi, T. (2022). Detection of the moldy status of the stored maize kernels using hyperspectral imaging and deep learning algorithms. *International Journal of Food Properties*, 25(1), 170-186.
- [18] Zhou, X., Sun, J., Tian, Y., Lu, B., Hang, Y., & Chen, Q. (2020). Development of deep learning method for lead content prediction of lettuce leaf using hyperspectral images. *International journal of remote sensing*, 41(6), 2263-2276.
- [19] Krishna, S. L., Jeya, I. J. S., & Deepa, S. N. (2022). Fuzzy-twin proximal SVM kernel-based deep learning neural network model for hyperspectral image classification. *Neural Computing and Applications*, 34(21), 19343-19376.
- [20] Çetin, N., Karaman, K., Kavuncuoğlu, E., Yıldırım, B., & Jahanbakhshi, A. (2022). Using hyperspectral imaging technology and machine learning algorithms for assessing internal quality parameters of apple fruits. *Chemometrics and Intelligent Laboratory Systems*, 230, 104650.
- [21] Wang, S., Guan, K., Wang, Z., Ainsworth, E. A., Zheng, T., Townsend, P. A., ... & Jiang, C. (2021). Airborne hyperspectral imaging of nitrogen deficiency on crop traits and yield of maize by machine learning and radiative transfer modeling. *International Journal of Applied Earth Observation and Geoinformation*, 105, 102617.
- [22] Rehman, T. U., Ma, D., Wang, L., Zhang, L., & Jin, J. (2020). Predictive spectral analysis using an end-to-end deep model from hyperspectral images for high-throughput plant phenotyping. *Computers and Electronics in Agriculture*, 177, 105713.